

# Chemical Science

rsc.li/chemical-science



ISSN 2041-6539



ROYAL SOCIETY  
OF CHEMISTRY

Celebrating  
IYPT 2019

## EDGE ARTICLE

Jinlong Gong *et al.*

Hydroxyl-mediated ethanol selectivity of CO<sub>2</sub> hydrogenation

Cite this: *Chem. Sci.*, 2019, 10, 3161

All publication charges for this article have been paid for by the Royal Society of Chemistry

Received 16th December 2018  
Accepted 11th February 2019

DOI: 10.1039/c8sc05608k

rsc.li/chemical-science

## Hydroxyl-mediated ethanol selectivity of CO<sub>2</sub> hydrogenation†

Chengsheng Yang,<sup>‡</sup> Rentao Mu,<sup>‡</sup> Guishuo Wang, Jimin Song, Hao Tian, Zhi-Jian Zhao and Jinlong Gong<sup>✉\*</sup>

Oxide-supported Rh nanoparticles have been widely used for CO<sub>2</sub> hydrogenation, especially for ethanol synthesis. However, this reaction operates under high pressure, up to 8 MPa, and suffers from low CO<sub>2</sub> conversion and alcohol selectivity. This paper describes the crucial role of hydroxyl groups bound on Rh-based catalysts supported on TiO<sub>2</sub> nanorods (NRs). The RhFeLi/TiO<sub>2</sub> NR catalyst shows superior reactivity ( $\approx 15\%$  conversion) and ethanol selectivity (32%) for CO<sub>2</sub> hydrogenation. The promoting effect can be attributed to the synergism of high Rh dispersion and high-density hydroxyl groups on TiO<sub>2</sub> NRs. Hydroxyls are proven to stabilize formate species and protonate methanol, which is easily dissociated into  $^*CH_x$ , and then CO obtained from the reverse water–gas shift reaction (RWGS) is inserted into  $^*CH_x$  to form CH<sub>3</sub>CO\*, followed by CH<sub>3</sub>CO\* hydrogenation to ethanol.

## Introduction

Carbon dioxide (CO<sub>2</sub>) is one of the major components of greenhouse gases, which can result in climate change and ocean acidification. Among the different approaches explored for controlling CO<sub>2</sub> emission, the chemical conversion of CO<sub>2</sub> to high-value-added fuels (oxygenates, alcohols, olefins *etc.*) has attracted extensive attention.<sup>1–4</sup> Compared with C<sub>1</sub> products (CO, CH<sub>4</sub> and CH<sub>3</sub>OH), the higher alcohols (C<sub>2+</sub>OH, especially C<sub>2</sub>H<sub>5</sub>OH), which are mostly produced from biological fermentation, are widely applied in industries as indispensable higher-energy-density engine fuels and fuel additives.<sup>1</sup> According to thermodynamic analysis, the formation of ethanol from CO<sub>2</sub> is limited enormously at 1–30 bar due to the preferential production of CO or CH<sub>4</sub>, thus the selectivity to ethanol is relatively low.<sup>4</sup>

Therefore, the production of C<sub>2+</sub>OH by CO<sub>2</sub> hydrogenation is appealing but remains very challenging. Previous studies have shown that a Pt/Co<sub>3</sub>O<sub>4</sub> catalyst<sup>5</sup> achieved 27.3% selectivity to C<sub>2+</sub>OH with H<sub>2</sub>O/DMI as a solvent. Multi-functional composite catalysts, such as CoMoS<sup>6</sup> (5.5% selectivity to ethanol), physically mixed Fe-based and Cu-based catalysts<sup>7</sup> (17.4% selectivity to ethanol) and K/Cu–Zn–Fe catalysts<sup>8,9</sup> (19.5% selectivity to C<sub>2+</sub>OH and CH<sub>3</sub>OH), were also used for alcohol synthesis. Particularly, Rh-based catalysts have been evaluated as

promising catalysts for the selective synthesis of ethanol.<sup>4,10,11</sup> In general, promoters such as Fe and Li are frequently used for enhancing ethanol selectivity *via* changing the electronic state of Rh and increasing the intensity of bridge-bonded CO species. For example, 5 wt% RhFe<sup>10</sup> and RhLi<sup>11</sup> supported on SiO<sub>2</sub> showed ethanol selectivities of 16.4% and 15.5%, respectively.

However, there are still some limitations for alcohol production through CO<sub>2</sub> hydrogenation reaction, such as the difficulties in CO<sub>2</sub> activation, high energy barrier for C–O bond scission and the formation of C<sub>1</sub> by-products.<sup>1</sup> Therefore, the design of efficient heterogeneous catalysts for ethanol production is of great importance. Tuning the particle size of noble metals can often increase the CO<sub>2</sub> conversion and product selectivity.<sup>12–16</sup> For example, suitable reducible metal oxide supports, such as TiO<sub>2</sub> and ZrO<sub>2</sub>, have been extensively applied to tune the particle size.<sup>17,18</sup> The Au/TiO<sub>2</sub> catalyst with abundant oxygen vacancies exhibited high selectivity to ethanol from CO<sub>2</sub> reduction in DMF solvent.<sup>19</sup> The bimetallic Pd<sub>2</sub>Cu/P25 catalyst also presented an excellent yield of ethanol with the help of water.<sup>20</sup> On the other hand, a promotion strategy *via* hydroxyl groups has also been proved to be an efficient approach towards improving alcohol selectivity in CO hydrogenation.<sup>21–23</sup>

This work shows that a high yield of ethanol under low pressure can be achieved by the introduction of hydroxyls onto a TiO<sub>2</sub> support. First, 1 wt% RhFeLi (Rh : Fe : Li = 1 : 1 : 1) catalysts supported on a series of reducible oxides were prepared. The catalysts supported on TiO<sub>2</sub> nanorods (NRs) display the highest selectivity to ethanol. Since TiO<sub>2</sub> NRs have been extensively used in a variety of catalytic systems, such as photocatalytic water splitting, CO<sub>2</sub> photoreduction and dissociation of CO<sub>2</sub> to CO,<sup>24–26</sup> we synthesized TiO<sub>2</sub> NRs by a modified hydrothermal method. More importantly, high-density surface

Key Laboratory for Green Chemical Technology of Ministry of Education, School of Chemical Engineering and Technology, Tianjin University, Collaborative Innovation Center of Chemical Science and Engineering, Tianjin 300072, China. E-mail: jlgong@tju.edu.cn

† Electronic supplementary information (ESI) available: Experimental details and supporting figures and tables. See DOI: 10.1039/c8sc05608k

‡ These authors contributed equally to this work.

hydroxyls can be introduced into the catalytic system after reduction of TiO<sub>2</sub> NR-supported catalysts in H<sub>2</sub>. A significant improvement of ethanol yield is observed for Rh-based catalysts supported on TiO<sub>2</sub> NRs, which have not been reported in previous studies. Furthermore, the hydroxyl-mediated mechanism of ethanol formation over RhFeLi/TiO<sub>2</sub> NRs catalysts is investigated.

## Results and discussion

### Catalyst structure

The morphology of the synthesized TiO<sub>2</sub> NRs is shown in Fig. 1a and S1.† The length and diameter of TiO<sub>2</sub> NRs are 50–200 nm and 10–20 nm, respectively. The specific surface area of TiO<sub>2</sub> NRs is determined to be 23.6 m<sup>2</sup> g<sub>cat</sub><sup>−1</sup>, which is close to that of commercial TiO<sub>2</sub> (TiO<sub>2</sub> Com, 18.2 m<sup>2</sup> g<sub>cat</sub><sup>−1</sup>) (Table S1†). The Rh-based catalysts supported on TiO<sub>2</sub> NRs and TiO<sub>2</sub> Com were prepared by incipient wetness impregnation. The Rh nanoparticles on TiO<sub>2</sub> NRs present uniform size distribution with an average diameter of 2.3 ± 1.0 nm (Fig. 1a, c and e). The high-resolution images of Rh nanoparticles shown in Fig. 1c and d present a lattice distance of 0.23 nm, corresponding to Rh (111) planes.<sup>27</sup> In contrast, two-times-larger (~4.0 nm) Rh nanoparticles in the range of 1–7 nm are observed on TiO<sub>2</sub> Com (Fig. 1b, d and f). TEM studies indicate that TiO<sub>2</sub> NRs can prevent the severe agglomeration of Rh nanoparticles after the reduction at 400 °C in a H<sub>2</sub> atmosphere.

In XRD measurements, no characteristic peak of Fe<sub>2</sub>O<sub>3</sub> can be found for RhFeLi/TiO<sub>2</sub> Com and RhFeLi/TiO<sub>2</sub> NRs when the

loading of Fe is relatively low (~1 wt%) (Fig. 2). When the loading of Fe is increased to 2.5 wt%, the diffraction peak of Fe<sub>2</sub>O<sub>3</sub> at 33.2° can be seen for TiO<sub>2</sub> Com. However, the diffraction peak of Fe<sub>2</sub>O<sub>3</sub> does not appear for TiO<sub>2</sub> NRs even though the loading of Fe is increased to 5 wt% (Fig. 2). XRD results indicate that the dispersion of FeO<sub>x</sub> over TiO<sub>2</sub> NRs is higher than that over TiO<sub>2</sub> Com. EDS elemental mapping of RhFeLi/TiO<sub>2</sub> NRs also shows that the FeO<sub>x</sub> species are well dispersed on TiO<sub>2</sub> NRs (Fig. 1g). We note that no Raman shift of TiO<sub>2</sub> can be observed for all catalysts (Fig. S2†), indicating that the FeO<sub>x</sub> species are deposited on the surface rather than being doped into TiO<sub>2</sub> bulk. The H<sub>2</sub> temperature-programmed reduction (H<sub>2</sub>-TPR) results of FeO<sub>x</sub>/TiO<sub>2</sub> show that the reduction temperature of FeO<sub>x</sub> over TiO<sub>2</sub> NRs is 100 °C higher than the reduction temperature of FeO<sub>x</sub> over TiO<sub>2</sub> Com (Fig. S3a†), suggesting that the FeO<sub>x</sub> species are better dispersed on TiO<sub>2</sub> NRs compared with TiO<sub>2</sub> Com.

H<sub>2</sub>-TPR studies of RhFeLi/TiO<sub>2</sub> NRs and RhFeLi/TiO<sub>2</sub> Com were also carried out to investigate the interfacial interaction between Rh and oxide promoters (Fig. S3b†). According to previous studies,<sup>10</sup> the peaks below 200 °C can be ascribed to the reduction of Rh<sub>2</sub>O<sub>3</sub>, while the broad peak appearing at higher temperature (300–500 °C) can be assigned to the reduction of Fe<sub>2</sub>O<sub>3</sub>. We find that the reduction temperature of Rh<sub>2</sub>O<sub>3</sub> for RhFeLi/TiO<sub>2</sub> NRs is 50 °C higher than that on RhFeLi/TiO<sub>2</sub> Com, illustrating smaller Rh size on TiO<sub>2</sub> NRs.<sup>14</sup> As such, the higher dispersion of Rh-based nanoparticles on TiO<sub>2</sub> NRs should increase the number of interfacial sites between Rh and oxide promoters, where C–C coupling occurs *via* reaction between CO and \*CH<sub>x</sub>.<sup>5–7</sup>

To further illustrate the surface structure of RhFeLi/TiO<sub>2</sub> NRs and RhFeLi/TiO<sub>2</sub> Com catalysts, CO titration experiments were

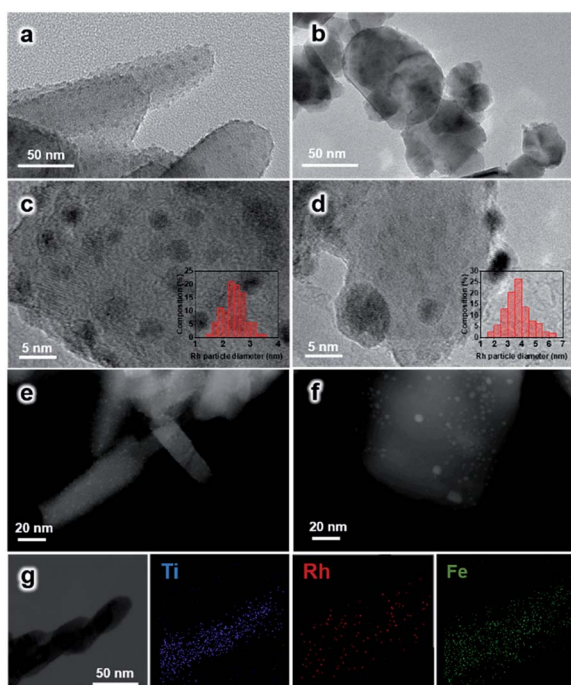


Fig. 1 (a and b) TEM; (c and d) HRTEM images, particle size distributions (inset figures) and (e and f) HAADF-STEM images of catalysts after reaction. (a, c and e) 2.5 wt% RhFeLi supported on TiO<sub>2</sub> NRs and (b, d and f) 2.5 wt% RhFeLi supported on TiO<sub>2</sub> Com. (g) STEM-EDS elemental mapping of 2.5 wt% RhFeLi supported on TiO<sub>2</sub> NRs.

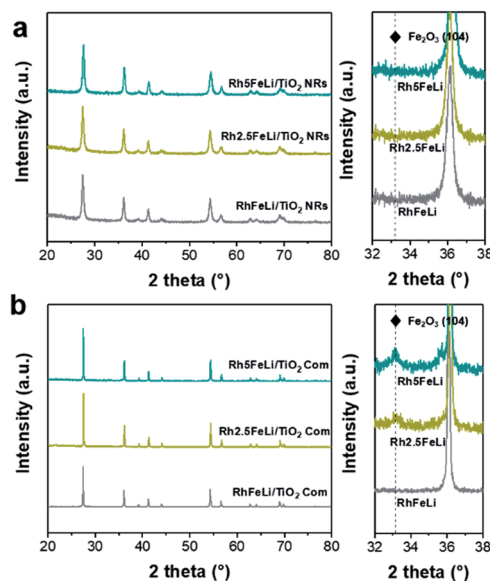


Fig. 2 (a) XRD spectra of 2.5 wt% RhFeLi/TiO<sub>2</sub> NRs with different Fe loadings. (b) XRD spectra of 2.5 wt% RhFeLi/TiO<sub>2</sub> Com with different Fe loadings. The figures on the right of (a) and (b) show the enlarged XRD patterns.





conducted. The active loop volume of CO for RhFeLi/TiO<sub>2</sub> Com (0.09 cm<sup>3</sup> g<sup>-1</sup>), which is consumed by CO adsorption on Rh, is much smaller than that for RhFeLi/TiO<sub>2</sub> NRs (0.69 cm<sup>3</sup> g<sup>-1</sup>) (Table S2†). The observed low adsorption amount of CO on RhFeLi/TiO<sub>2</sub> Com may be due to the partial encapsulation of Rh sites by oxide overlayers. The TEM image also shows that the Rh nanoparticles are decorated by oxide overlayers in the RhFeLi/TiO<sub>2</sub> Com catalyst (Fig. 1d). Quantitative XPS analysis was also conducted to investigate the surface structure of Rh-based catalysts (Table S3†). The surface molar ratio of Rh : Fe in RhFeLi/TiO<sub>2</sub> NRs is determined to be 58 : 42, which is close to the bulk molar ratio of Rh : Fe measured by ICP-AES (48 : 52) and the initial feed ratio. For RhFeLi/TiO<sub>2</sub> Com, XPS investigations show that the surface molar ratio of Rh : Fe is 29 : 71. However, the bulk molar ratio of Rh : Fe determined by ICP-AES (Rh : Fe = 50 : 50) still agrees with the initial feed ratio, suggesting that the Rh nanoparticles should be partially covered by the FeO<sub>x</sub> species. Note that the binding energy (BE) of Rh 3d<sub>5/2</sub> locates at ~307.0 eV (Fig. S4b†), corresponding to the metallic state of Rh.<sup>28</sup>

### Catalytic performance

The catalytic performance of Rh-based catalysts supported on different oxide supports in CO<sub>2</sub> hydrogenation is studied. The TiO<sub>2</sub> NR-supported catalysts present the highest ethanol yield (Fig. S5†). Additionally, a series of Rh-based catalysts with different promoters were synthesized. Compared with the mono-component Rh/TiO<sub>2</sub> catalyst, the selectivity of RhFe/TiO<sub>2</sub> for ethanol is improved significantly (16% for RhFe/TiO<sub>2</sub> Com and 25% for RhFe/TiO<sub>2</sub> NRs, Fig. S6†). With an increase of the loading of Fe, CO<sub>2</sub> conversion and the selectivity to ethanol and CH<sub>4</sub> decreased while the selectivity to CO increased (Fig. S7†). Since FeO<sub>x</sub> could catalyze the reverse water-gas shift reaction (RWGS) to produce CO, the changes of CO<sub>2</sub> conversion and product distribution indicate that the excess Fe species has a passive effect on CO<sub>2</sub> conversion and ethanol synthesis by blocking the active Rh sites.<sup>10</sup> This blocking effect may be caused by the encapsulation of Rh sites by FeO<sub>x</sub> species, which has been proven by XPS measurements combined with CO chemisorption (Table S2†). On the other hand, the addition of Li can increase the CO<sub>2</sub> conversion on Rh/TiO<sub>2</sub> by 5%, while the selectivity to ethanol does not change (Fig. S6c†). Based on these results, we conclude that the addition of Fe can promote the ethanol selectivity, while the addition of Li as an electronic promoter accelerates the CO<sub>2</sub> conversion. As such, higher ethanol selectivity and CO<sub>2</sub> conversion are obtained by adding binary promoters *i.e.*, Fe and Li (Fig. S6d†).

More interestingly, we show that the ethanol selectivity and CO<sub>2</sub> conversion over RhFeLi/TiO<sub>2</sub> NRs are much higher than those over RhFeLi/TiO<sub>2</sub> Com at 250 °C (Fig. S7†). For example, the 2.5 wt% RhFeLi/TiO<sub>2</sub> NR (Rh : Fe : Li = 1 : 1 : 1) catalyst presents more than 30% ethanol selectivity and 15% CO<sub>2</sub> conversion, which is about seven-fold higher ethanol yield than that on 2.5 wt% RhFeLi/TiO<sub>2</sub> Com (Fig. 3). The catalytic performance of RhFeLi/TiO<sub>2</sub> NRs remains stable in a 20 h stability test (Fig. S7†). The superior reactivity and long-term

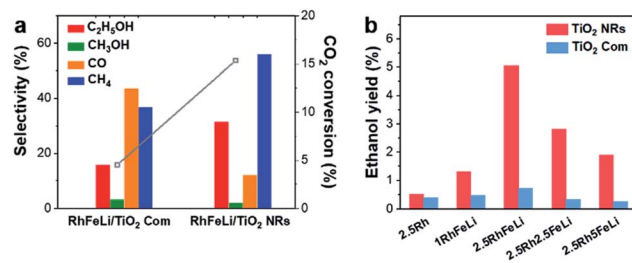


Fig. 3 (a) The CO<sub>2</sub> conversion (grey) and product selectivity of 2.5 wt% RhFeLi/TiO<sub>2</sub> NRs and 2.5 wt% RhFeLi/TiO<sub>2</sub> Com. (b) The ethanol yield of the Rh-based catalyst supported on TiO<sub>2</sub> NRs and TiO<sub>2</sub> Com.

stability of RhFeLi/TiO<sub>2</sub> NRs catalysts provide an inspiration for their potential industrial application.

### Promotion effects of the hydroxyl groups

First, the hydroxyl groups were introduced by pre-reduction of RhFeLi/TiO<sub>2</sub> NRs and RhFeLi/TiO<sub>2</sub> Com catalysts in a H<sub>2</sub> atmosphere at 400 °C. Fourier transform infrared (FTIR) experiments were carried out to characterize the surface hydroxyl groups on RhFeLi/TiO<sub>2</sub> catalysts. As shown in Fig. S8,† the broad band at 3450 cm<sup>-1</sup> and the sharp peak at 1640 cm<sup>-1</sup> are assigned to the stretching and bending vibrations of associated hydroxyls, respectively.<sup>29</sup> The density of hydroxyl groups on RhFeLi/TiO<sub>2</sub> NRs is much higher than that on RhFeLi/TiO<sub>2</sub> Com (Fig. 4a), suggesting that high-density hydroxyl groups could be introduced into the catalytic system by using TiO<sub>2</sub> NRs. Subsequently, the catalytic properties of the hydroxyls on TiO<sub>2</sub>

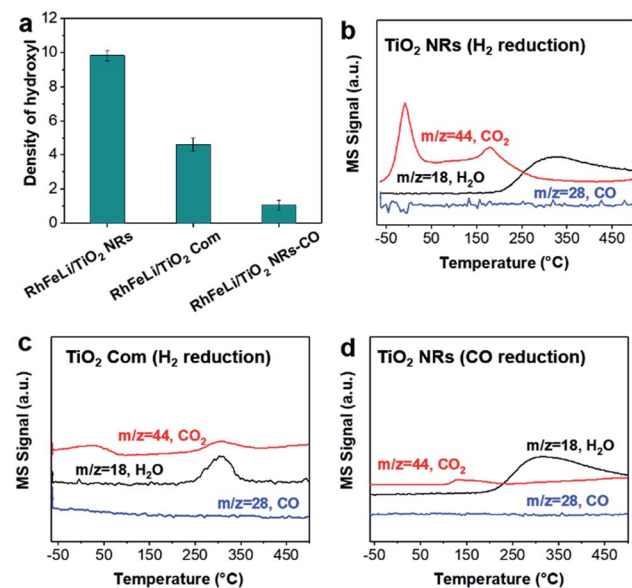


Fig. 4 (a) The peak area of hydroxyls in FTIR normalized by S<sub>BET</sub> (×10<sup>3</sup>) on 2.5 wt% RhFeLi/TiO<sub>2</sub> NRs, 2.5 wt% RhFeLi/TiO<sub>2</sub> Com and 2.5 wt% RhFeLi/TiO<sub>2</sub> NRs-CO. (b) CO-TPD profiles of 2.5 wt% RhFeLi/TiO<sub>2</sub> NRs. Pretreatment: H<sub>2</sub> reduction at 400 °C. (c) CO-TPD profiles of 2.5 wt% RhFeLi/TiO<sub>2</sub> Com. Pretreatment: H<sub>2</sub> reduction at 400 °C. (d) CO-TPD profiles of 2.5 wt% RhFeLi/TiO<sub>2</sub> NRs. Pretreatment: CO reduction at 350 °C.

NRs are characterized by CO temperature-programmed desorption (CO-TPD). A sharp signal peak of CO<sub>2</sub> ( $m/z = 44$ ) at  $\sim 0^\circ\text{C}$  is observed in CO-TPD profiles for both RhFeLi/TiO<sub>2</sub> NRs and pure TiO<sub>2</sub> NRs (Fig. 4b and S8a†). As reported previously, the CO<sub>2</sub> may originate from the water-gas shift process, in which the CO adsorbed on Rh sites reacts with hydroxyl groups.<sup>29,30</sup> However, a small CO<sub>2</sub> peak at  $\sim 0^\circ\text{C}$  is observed for RhFeLi/TiO<sub>2</sub> Com and pure TiO<sub>2</sub> Com due to the lack of hydroxyls (Fig. 4c and S8a†).

The TOF of ethanol formed over RhFeLi/TiO<sub>2</sub> NRs is determined to be  $0.12\text{ h}^{-1}$ , which is much higher than that over RhFeLi/TiO<sub>2</sub> Com or RhFeLi/SiO<sub>2</sub> ( $0.08\text{ h}^{-1}$ ) (Table S2†). Therefore, we suggest that the surface hydroxyl groups may play an important role in ethanol formation *via* CO<sub>2</sub> hydrogenation. To verify the role of hydroxyls in ethanol formation, the RhFeLi/TiO<sub>2</sub> NR catalyst was pre-treated in a CO atmosphere (RhFeLi/TiO<sub>2</sub> NRs-CO). The removal process of hydroxyl groups in CO was monitored by *in situ* diffuse reflectance infrared Fourier transform spectroscopy (DRIFTS, Fig. S9a†).<sup>31</sup> We find that the IR peak of hydroxyl stretching vibrations ( $3450\text{ cm}^{-1}$ ) disappears gradually in CO at  $350^\circ\text{C}$ . The hydroxyls can be removed completely after  $\sim 12$  minutes of CO-feeding (Fig. S9b†). After the pre-treatment in CO flow at  $350^\circ\text{C}$ , the CO<sub>2</sub> peak at  $\sim 0^\circ\text{C}$  isn't observed in the CO-TPD profile (Fig. 4d), and RhFeLi/TiO<sub>2</sub> NR-CO catalysts with a hydroxyl-deficient surface are prepared (Fig. 4a and S8b†). Compared with RhFeLi/TiO<sub>2</sub> NRs reduced with H<sub>2</sub>, the RhFeLi/TiO<sub>2</sub> NRs-CO catalyst exhibits much lower CO<sub>2</sub> conversion (4.7%) and produces almost no ethanol (Fig. 5a). The selectivity to CO reaches  $\sim 80\%$  among the products and the selectivity to CH<sub>4</sub> decreases from 53.9% to 9.6%. In the TEM images (Fig. S10†), RhFeLi/TiO<sub>2</sub> NRs and RhFeLi/TiO<sub>2</sub>

NR-CO catalysts show similar size distribution. Besides, there is no BE shift of the XPS Rh 3d peak for RhFeLi/TiO<sub>2</sub> NR-CO compared with RhFeLi/TiO<sub>2</sub> NRs (Fig. S11, Table S4†). Therefore, the influences of the size effect and chemical state of Rh can be excluded. Instead, the decrease of the selectivity to CH<sub>4</sub> and ethanol should be attributed to the lack of hydroxyls. When hydroxyl groups are re-introduced by H<sub>2</sub> exposure (Fig. 5b and S8b†), promoted catalytic performance is achieved (35% ethanol selectivity and 18% CO<sub>2</sub> conversion), which is very similar to that of fresh RhFeLi/TiO<sub>2</sub> NRs reduced with H<sub>2</sub>. These results further indicate that hydroxyls play an important role in tuning product distribution and promoting ethanol synthesis through CO<sub>2</sub> hydrogenation.

In sequential experiments, a mixture of CO<sub>2</sub> and H<sub>2</sub> (CO<sub>2</sub> : H<sub>2</sub> = 1 : 3) is first introduced into an *in situ* cell at  $250^\circ\text{C}$ , followed by a switch to pure CO<sub>2</sub> flow to investigate the stability of hydroxyls and formate species. In a CO<sub>2</sub> + H<sub>2</sub> atmosphere (CO<sub>2</sub> : H<sub>2</sub> = 1 : 3) at  $250^\circ\text{C}$ , the bands at  $3016$ ,  $2965$  and  $2880\text{ cm}^{-1}$  in the  $\nu_{\text{C-H}}$  region appear to be stemming from gaseous CH<sub>4</sub> ( $3016\text{ cm}^{-1}$ ) and adsorbed formate species, respectively. In the O-C-O stretching region between  $1650$  and  $1200\text{ cm}^{-1}$ , the bands at  $1520$  and  $1390\text{ cm}^{-1}$  are assigned to carbonate, while the rest of the peaks may stem from adsorbed formate ( $1595$  and  $1370\text{ cm}^{-1}$ , Table S5†).<sup>32–34</sup> The absorbance intensities of the dissociated hydroxyl stretching vibrations at  $3600\text{ cm}^{-1}$  and OCO asymmetric stretching vibration at  $1595\text{ cm}^{-1}$  in DRIFTS are used to represent the amount of hydroxyls and formate, respectively.<sup>34</sup> As shown in Fig. 6, the changes of the hydroxyl amount and the formate amount are plotted as a function of time when switching the CO<sub>2</sub> + H<sub>2</sub> flow to pure CO<sub>2</sub> flow at  $250^\circ\text{C}$ . We find that the amounts of hydroxyls and formate species on RhFeLi/TiO<sub>2</sub> NRs remain almost unchanged under pure CO<sub>2</sub> flow for 40 min (Fig. 6, S12a and c†). In contrast, the hydroxyls and formate adsorbed on RhFeLi/TiO<sub>2</sub> Com disappear rapidly within 20 min (Fig. 6, S12b and d†). We suggest that the abundant hydroxyl groups on RhFeLi/TiO<sub>2</sub> NRs can stabilize the formate species, which has been proposed to be one of the intermediates of methanation *via* formate hydrogenation and then scission of C-O in  $^*\text{CH}_x\text{-O}$ .<sup>18,35</sup>

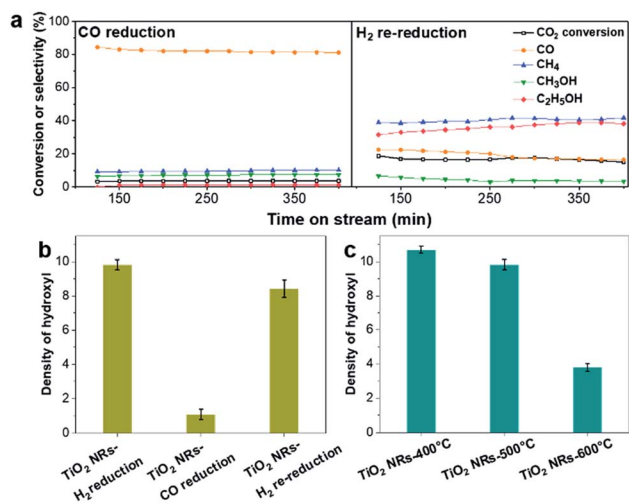


Fig. 5 (a) CO<sub>2</sub> conversion and product selectivity *versus* time obtained from 2.5 wt% RhFeLi/TiO<sub>2</sub> NRs. CO reduction was conducted at  $350^\circ\text{C}$  for 0.5 h. Re-reduction in H<sub>2</sub> was carried out at  $400^\circ\text{C}$  for 1 h. Reaction conditions:  $P = 30\text{ atm}$ ,  $T = 250^\circ\text{C}$ ,  $\text{GHSV} = 6000\text{ h}^{-1}$ ,  $\text{CO}_2/\text{H}_2 = 1/3$ . (b) The peak area of hydroxyls in FTIR normalized by  $S_{\text{BET}}$  ( $\times 10^3$ ) on 2.5 wt% RhFeLi/TiO<sub>2</sub> NRs pretreated under different reduction atmospheres. (c) The peak area of hydroxyls in FTIR normalized by  $S_{\text{BET}}$  ( $\times 10^3$ ) on 2.5 wt% RhFeLi/TiO<sub>2</sub> NRs calcined at different temperatures.

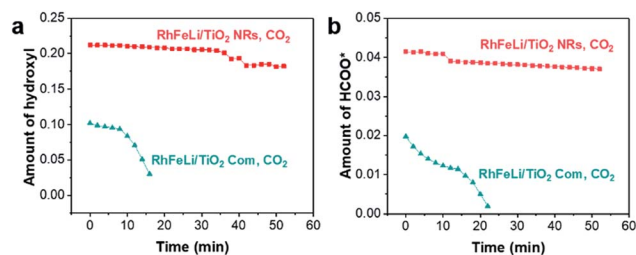
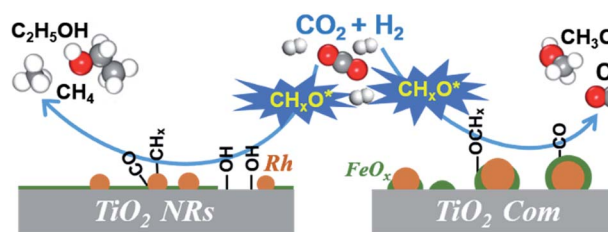


Fig. 6 (a) The absorbance intensity of hydroxyls at  $3600\text{ cm}^{-1}$  in DRIFTS of 2.5 wt% RhFeLi/TiO<sub>2</sub> NRs and 2.5 wt% RhFeLi/TiO<sub>2</sub> Com *versus* time after switching the CO<sub>2</sub> + H<sub>2</sub> + Ar (CO<sub>2</sub> : H<sub>2</sub> = 1 : 3) flow to pure CO<sub>2</sub> flow at  $250^\circ\text{C}$ . (b) The absorbance intensity of formate at  $1595\text{ cm}^{-1}$  in DRIFTS of 2.5 wt% RhFeLi/TiO<sub>2</sub> NRs and 2.5 wt% RhFeLi/TiO<sub>2</sub> Com *versus* time after switching the CO<sub>2</sub> + H<sub>2</sub> + Ar (CO<sub>2</sub> : H<sub>2</sub> = 1 : 3) flow to pure CO<sub>2</sub> flow at  $250^\circ\text{C}$ .



*In situ* DRIFTS was further carried out to investigate the catalytic role of hydroxyls in ethanol formation. In contrast to RhFeLi/TiO<sub>2</sub> Com, additional bands at 1470 cm<sup>-1</sup> and 1746 cm<sup>-1</sup> are observed for RhFeLi/TiO<sub>2</sub> NRs under a CO<sub>2</sub> + H<sub>2</sub> atmosphere (CO<sub>2</sub> : H<sub>2</sub> = 1 : 3) at 250 °C (Fig. 7a). The existence of the band at 1746 cm<sup>-1</sup> has been reported for Rh/Al<sub>2</sub>O<sub>3</sub> (ref. 35) and Ru/Al<sub>2</sub>O<sub>3</sub> (ref. 36) catalysts, which can be attributed to adsorbed formyl (CHO\*) species. It is believed that the formation of CHO\* is the rate-limiting step of ethanol synthesis (Scheme S1†).<sup>12</sup> Also, CHO\* is thermodynamically more favored to be dissociated into \*CH<sub>x</sub> than into CO.<sup>21–23,37</sup> As expected, significant amounts of \*CH<sub>3</sub> species (1470 cm<sup>-1</sup>) are observed on the surface of RhFeLi/TiO<sub>2</sub> NRs (Fig. 7a).<sup>17,18</sup> Subsequently, CO can be inserted into these abundant adsorbed \*CH<sub>3</sub> species on RhFeLi/TiO<sub>2</sub> NRs, which may be responsible for the high ethanol yield.<sup>38</sup> Based on the above analysis, a mechanism that hydroxyls stabilize the formate and accelerate the scission of CH<sub>x</sub>-O to produce \*CH<sub>3</sub> species is proposed (Scheme 1).

With increasing the calcination temperature from 400 to 600 °C, the normalized peak area of associated hydroxyl vibration bands for RhFeLi/TiO<sub>2</sub> NRs decreases gradually, indicating that the density of hydroxyls is decreased (Fig. 5c and S8c†). In addition, the summed selectivity and TOF of CH<sub>4</sub> and ethanol show a downward trend with increasing the calcination temperature of TiO<sub>2</sub> NRs (Tables S2 and S6†). Since the RhFeLi nanoparticles show a similar size distribution (Fig. S10†) and the same electronic state of Rh and Fe as that for TiO<sub>2</sub> NRs calcined at various temperatures (Fig. S11, Table S4†), the



Scheme 1 Schematic of CO<sub>2</sub> hydrogenation over the Rh-based catalyst with or without hydroxyl groups on TiO<sub>2</sub>. The hydroxyls play an important role in accelerating the scission of CH<sub>x</sub>-O\* and promote the formation of ethanol.

differences in catalytic performance should be attributed to the changes of surface hydroxyls. It is noteworthy that the catalytic performance of RhFeLi/TiO<sub>2</sub> NRs-600 °C is comparable to that of the RhFeLi/TiO<sub>2</sub> NRs-CO catalyst, because there are few hydroxyls on their surfaces. Similarly, changing the support from TiO<sub>2</sub> NRs to TiO<sub>2</sub> Com can also generate a hydroxyl-deficient surface, causing the selectivity for ethanol and CH<sub>4</sub> to be reduced largely (Table S6†). To display the relationship between hydroxyl groups and catalytic performance directly, we take the summed amount of CH<sub>4</sub> and ethanol as the total amount of \*CH<sub>3</sub>, because these two products stem from \*CH<sub>3</sub> hydrogenation and CO insertion, respectively.<sup>39</sup> As shown in Fig. 7b, the amount of \*CH<sub>3</sub> exhibits a linear correlation with the density of hydroxyls, illustrating that hydroxyls may accelerate the scission of the C-O bond to form the \*CH<sub>3</sub> species.

The reactions of CH<sub>3</sub>OH and H<sub>2</sub> over RhFeLi/TiO<sub>2</sub> were conducted as well to elucidate the role of hydroxyls. The DRIFTS data were obtained after pre-treatment with CH<sub>3</sub>OH and subsequent feeding with H<sub>2</sub> at 250 °C (Fig. 7c). Upon the feeding of CH<sub>3</sub>OH, all the samples show similar CH<sub>3</sub>O\* (2825 and 2927 cm<sup>-1</sup>) species.<sup>40–42</sup> After the feeding of H<sub>2</sub>, the IR peak intensity of CH<sub>3</sub>O\* in RhFeLi/TiO<sub>2</sub> NRs decreases. Simultaneously, an obvious IR peak of gaseous CH<sub>4</sub> (3016 cm<sup>-1</sup>) can be observed for RhFeLi/TiO<sub>2</sub> NRs. The formation of CH<sub>4</sub> could be attributed to the C-O bond scission in CH<sub>3</sub>O\* followed by \*CH<sub>3</sub> hydrogenation. The hydroxyl groups on RhFeLi/TiO<sub>2</sub> NRs are suggested to promote the C-O bond scission in CH<sub>3</sub>O\* to produce the \*CH<sub>3</sub> intermediate. In contrast, the IR peak intensity of CH<sub>3</sub>O\* does not decrease, and CH<sub>4</sub> is hardly found for RhFeLi/TiO<sub>2</sub> Com and RhFeLi/TiO<sub>2</sub> NRs-CO after H<sub>2</sub> feeding. Therefore, it is reasonable to infer that the hydroxyls on RhFeLi/TiO<sub>2</sub> NRs could protonate CH<sub>3</sub>O\*, *i.e.*, promoting C-O bond scission in CH<sub>3</sub>O\* to form \*CH<sub>3</sub>. A similar phenomenon is observed under CO and H<sub>2</sub> at 250 °C (Fig. 7d). A sharp CH<sub>4</sub> peak emerges for RhFeLi/TiO<sub>2</sub> NRs, which is accompanied by formate (2880 and 2965 cm<sup>-1</sup>) and CH<sub>3</sub>O\* (2825 and 2927 cm<sup>-1</sup>). In contrast, we find only CH<sub>3</sub>O\* species adsorbed on RhFeLi/TiO<sub>2</sub> NRs-CO. The IR peaks of gaseous CH<sub>4</sub> and formate are undetectable for RhFeLi/TiO<sub>2</sub> NRs-CO and RhFeLi/TiO<sub>2</sub> Com, which could be attributed to the removal of hydroxyls after CO treatment.

Previous studies have proposed that ethanol can be synthesized by CO insertion into \*CH<sub>3</sub> species to form CH<sub>3</sub>CO\*, followed by CH<sub>3</sub>CO\* hydrogenation.<sup>37,38</sup> To verify this route of ethanol formation, the DRIFTS data of RhFeLi/TiO<sub>2</sub> NRs and

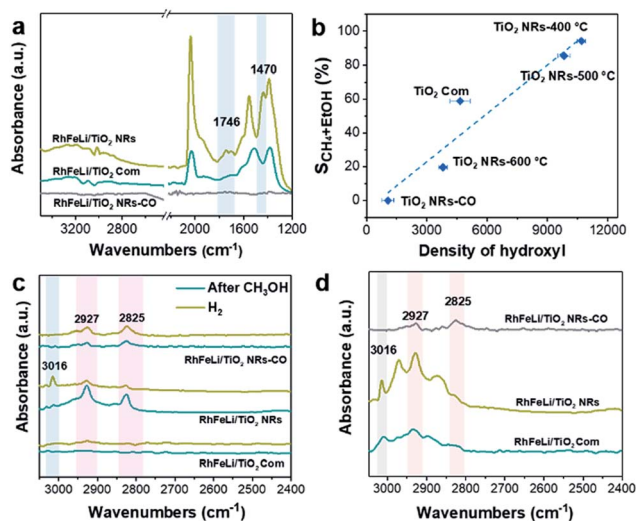


Fig. 7 (a) *In situ* DRIFTS of 2.5 wt% RhFeLi/TiO<sub>2</sub> NRs, 2.5 wt% RhFeLi/TiO<sub>2</sub> Com and 2.5 wt% RhFeLi/TiO<sub>2</sub> NRs-CO under a CO<sub>2</sub> + H<sub>2</sub> + Ar (CO<sub>2</sub> : H<sub>2</sub> = 1 : 3) atmosphere at 250 °C. (b) The summed selectivity to CH<sub>4</sub> and ethanol as a function of the peak area of hydroxyls normalized by S<sub>BET</sub> of the samples obtained from 2.5 wt% RhFeLi supported on different TiO<sub>2</sub> supports. (c) *In situ* DRIFTS of 2.5 wt% RhFeLi/TiO<sub>2</sub> NRs, 2.5 wt% RhFeLi/TiO<sub>2</sub> Com and 2.5 wt% RhFeLi/TiO<sub>2</sub> NRs-CO after CH<sub>3</sub>OH + Ar adsorption followed by H<sub>2</sub> adsorption at 250 °C. (d) *In situ* DRIFTS of 2.5 wt% RhFeLi/TiO<sub>2</sub> NRs, 2.5 wt% RhFeLi/TiO<sub>2</sub> Com and 2.5 wt% RhFeLi/TiO<sub>2</sub> NRs-CO under a CO + H<sub>2</sub> + Ar (CO : H<sub>2</sub> = 1 : 2) atmosphere at 250 °C.





RhFeLi/TiO<sub>2</sub> NRs-CO were obtained after pre-treatment with CH<sub>3</sub>OH and subsequent feeding with CO + H<sub>2</sub> (CO : H<sub>2</sub> = 1 : 1) at 250 °C (Fig. S13a†). Both gaseous and liquid products were analyzed in the reaction of CH<sub>3</sub>OH + CO + H<sub>2</sub> at 250 °C (Fig. S13b†), and ethanol is the only C<sub>2+</sub> product. Hence, the appearance of the methylene peak (2858 cm<sup>-1</sup>) for RhFeLi/TiO<sub>2</sub> NRs indicates the C–C coupling and formation of ethanol.<sup>43</sup> However, methylene, *i.e.*, ethanol is not formed over RhFeLi/TiO<sub>2</sub> NRs-CO. According to these data, the high ethanol selectivity of RhFeLi/TiO<sub>2</sub> NRs might be attributed to the high-density hydroxyls, which enhance the C–O bond scission to produce \*CH<sub>x</sub> intermediates for the CO insertion.

Surface functionalization with hydroxyls is frequently applied to promote the catalytic performance of catalysts.<sup>44–47</sup> The role of surface hydroxyls has often been considered to modulate the local concentration of hydrophilic reactants, such as alcohols, around the active sites. For example, the hydrophobic treatment of Pd/MOF improves its catalytic activity for styrene hydrogenation by increasing the interaction between hydrophobic reactants and Pd sites.<sup>48</sup> In formaldehyde oxidation reaction, the abundant hydroxyl groups nearby the Pt active sites can also facilitate formate oxidation through the formation of the Pt/Ni(OH)<sub>x</sub> interface.<sup>49</sup> In CO<sub>2</sub> hydrogenation reaction, hydroxyl groups on hydrophilic SiC quantum dots can promote methanol formation *via* a H-transfer mechanism, in which the diffusion of H from hydroxyl groups to CO<sub>2</sub> assists the formation of the intermediate HCOO\*.<sup>50</sup> Here, our work clearly demonstrates the catalytic role of hydroxyl groups in ethanol synthesis *via* CO<sub>2</sub> hydrogenation. We show that the surface hydroxyl species on RhFeLi/TiO<sub>2</sub> NRs can protonate methanol and reduce the energy barrier for C–O bond scission, facilitating the generation of \*CH<sub>3</sub> species. Accordingly, CO obtained from RWGS can be inserted into abundant \*CH<sub>3</sub> species to form CH<sub>3</sub>CO\*, followed by CH<sub>3</sub>CO\* hydrogenation to ethanol.

## Conclusions

In conclusion, we have demonstrated the crucial role of surface hydroxyls on the RhFeLi/TiO<sub>2</sub> NR catalyst in the synthesis of ethanol from CO<sub>2</sub> hydrogenation. Based on *in situ* spectroscopic characterization, we propose two advantages of the TiO<sub>2</sub> NR support for CO<sub>2</sub> hydrogenation to ethanol: (i) Rh-based nanoparticles are highly dispersed on TiO<sub>2</sub> NRs due to the strong interaction between the catalyst and TiO<sub>2</sub> NR support, thus displaying high activity; (ii) abundant hydroxyls on TiO<sub>2</sub> NRs can protonate methanol, which is easily dissociated into \*CH<sub>x</sub>, thus favoring the formation of ethanol upon CO insertion. This work not only provides the detailed understanding of the catalytic role of hydroxyls in heterogeneous catalysis but also opens an avenue for developing efficient catalysts for CO<sub>2</sub> conversion.

## Experimental section

### Chemicals

TiO<sub>2</sub> NRs were prepared by hydrothermal treatment of a mixture of titanium tetrachloride, nitric acid and water.<sup>51,52</sup> Briefly,

titanium tetrachloride (TiCl<sub>4</sub>, Shanghai Chemical Reagent Co., 98%) was dissolved in ultrapure water in an ice-water bath to obtain a 3 M TiCl<sub>4</sub> solution. Subsequently, 35 mL aliquot of concentrated nitric acid (HNO<sub>3</sub>, 15 M) was refluxed in a silicone oil bath and heated to 200 °C gradually, and then 20 mL of the 3 M titanium tetrachloride solution was rapidly injected into nitric acid under vigorous stirring. After aging for 20 h, the autoclave was cooled to room temperature. The obtained precipitates were centrifuged and washed several times with deionized water and ethanol. The filtered solid was dried at 100 °C in a vacuum overnight and calcined at 300, 400, 500 and 600 °C for 4 h, respectively (denoted as TiO<sub>2</sub> NRs-*x* °C). Unless otherwise specified, TiO<sub>2</sub> NRs are denoted as TiO<sub>2</sub> NRs-500 °C. The commercial TiO<sub>2</sub> (TiO<sub>2</sub> Com) was purchased from Alfa Aesar Chemical Co. Ltd for comparison.

RhCl<sub>3</sub>·*n*H<sub>2</sub>O (Huaweiruike Chemical Co., 99%), LiNO<sub>3</sub> (Alfa Aesar Chemical Co. Ltd., 98%) and Fe(NO<sub>3</sub>)<sub>3</sub>·9H<sub>2</sub>O (Alfa Aesar Chemical Co. Ltd., 98%) were used as precursors and a series of reducible metal oxides (MO) were used as the support. MO (1 g) were impregnated with distilled water (1 mL) containing the precursor by using ultrasonication for 1 h. Generally, the molar ratio of Rh and promoters was 1 : 1 unless specified. Subsequently, the sample was dried at room temperature overnight and then at 80 °C for 10 h. Finally, the sample was calcined in air at 300–500 °C for 4 h and reduced in pure H<sub>2</sub> at 400 °C for 2 h. The element loading was based on the weight ratio of Rh and Fe with respect to MO supports.

### Hydrogenation of CO<sub>2</sub>

All the catalytic reactions were carried out in a fixed-bed micro-reactor. In a typical experiment, 300 mg of each catalyst with a 20–40 mesh size distribution was mixed with 2.0 g of quartz particles (SiC: granulation of 0.075–0.4 mm) to avoid hot spots and pressure drop across the bed and packed in a stainless steel ( $\phi$  8 × 400 mm) tubular reactor. Prior to each experiment, the catalyst was activated by reduction in a H<sub>2</sub> atmosphere (99.99%) with a flow rate of 30 mL min<sup>-1</sup> and a temperature of 400 °C for 1 h. The RhFeLi/TiO<sub>2</sub> NRs-CO sample was obtained from RhFeLi/TiO<sub>2</sub> NRs-500 °C reduced under CO flow at 350 °C for 0.5 h. After the reduction of the catalyst, the reactor was cooled down to reaction temperature. Then the reactant gases (CO<sub>2</sub> and H<sub>2</sub> with a molar ratio of 1 : 3, 30 bar) were introduced into the reactor. The gas hourly space velocity (GHSV) was set at 6000 h<sup>-1</sup>. The product gas was analyzed with an online gas chromatograph (GC, Agilent 7890B) equipped with two detectors. One is a flame ionization detector (FID) with a HP-FFAP column using H<sub>2</sub> as a carrier gas to analyze the organic species such as alcohols, oxygenates and hydrocarbons. The other one is a thermal conductivity detector (TCD) with columns of MS-5A and Hayesep Q using He as a carrier gas to monitor the non-condensable gas species including H<sub>2</sub>, CO<sub>2</sub>, N<sub>2</sub>, CO and CH<sub>4</sub>. All the flows between the reactor and the GC were heated and maintained beyond 150 °C, to avoid the liquefaction of the alcohol products.

## Conflicts of interest

There are no conflicts to declare.



## Acknowledgements

This work was financially supported by the National Key R&D Program of China (2016YFB0600901), the National Natural Science Foundation of China (21525626, 21603159, 21676181), and the Program of Introducing Talents of Discipline to Universities (B06006).

## References

- 1 M. Aresta, A. Dibenedetto and A. Angelini, *Chem. Rev.*, 2014, **114**, 1709–1742.
- 2 W. Wang, S. Wang, X. Ma and J. Gong, *Chem. Soc. Rev.*, 2011, **40**, 3703–3727.
- 3 H. Yang, C. Zhang, P. Gao, H. Wang, X. Li, L. Zhong, W. Wei and Y. Sun, *Catal. Sci. Technol.*, 2017, **7**, 4580–4598.
- 4 A. Swapnesh, V. C. Srivastava and I. D. Mall, *Chem. Eng. Technol.*, 2014, **37**, 1765–1777.
- 5 Z. He, Q. Qian, J. Ma, Q. Meng, H. J. Zhou, H. J. Song, Z. Liu and B. Han, *Angew. Chem., Int. Ed.*, 2016, **128**, 747–751.
- 6 D. L. S. Nieskens, D. Ferrari, Y. Liu and R. Kolonko, *Catal. Commun.*, 2011, **14**, 111–113.
- 7 T. Inui, T. Yamamoto, M. Inoue, H. Hara, T. Takeguchi and J. B. Kim, *Appl. Catal., A*, 1999, **186**, 395–406.
- 8 M. Takagawa, A. Okamoto, H. Fujimura, Y. Izawa and H. Arakawa, *Stud. Surf. Sci. Catal.*, 1998, **114**, 525–528.
- 9 S. Li, H. Guo, C. Luo, H. Zhang, L. Xiong, X. Chen and L. Ma, *Catal. Lett.*, 2013, **143**, 345–355.
- 10 H. Kusama, K. Okabe, K. Sayama and H. Arakawa, *Energy*, 1997, **22**, 343–348.
- 11 H. Kusama, K. Okabe, K. Sayama and H. Arakawa, *Catal. Today*, 1996, **28**, 261–266.
- 12 Y. Choi and P. Liu, *J. Am. Chem. Soc.*, 2009, **131**, 13054–13061.
- 13 N. Yang, A. J. Medford, X. Liu, F. Studt, T. Bligaard, S. F. Bent and J. K. Nørskov, *J. Am. Chem. Soc.*, 2016, **138**, 3705–3714.
- 14 Y. Wang, H. Luo, D. Liang and X. Bao, *J. Catal.*, 2000, **196**, 46–55.
- 15 R. G. Zhang, M. Peng and B. J. Wang, *Catal. Sci. Technol.*, 2017, **7**, 1073–1085.
- 16 J. C. Matsubu, V. N. Yang and P. Christopher, *J. Am. Chem. Soc.*, 2015, **137**, 3076–3084.
- 17 S. Kattel, W. Yu, X. Yang, B. Yan, Y. Huang, W. Wan, P. Liu and J. G. Chen, *Angew. Chem., Int. Ed.*, 2016, **55**, 7968–7973.
- 18 S. Kattel, P. Liu and J. G. Chen, *J. Am. Chem. Soc.*, 2017, **139**, 9739–9754.
- 19 D. Wang, Q. Bi, G. Yin, W. Zhao, F. Huang, X. Xie and M. Jiang, *Chem. Commun.*, 2016, **52**, 14226–14229.
- 20 S. Bai, Q. Shao, P. Wang, Q. Dai, X. Wang and X. Huang, *J. Am. Chem. Soc.*, 2017, **139**, 6827–6830.
- 21 R. Burch and M. J. Hayes, *J. Catal.*, 1997, **165**, 249–261.
- 22 J. Xu, X. Su, H. Duan, B. Hou, Q. Lin, X. Liu, X. Pan, G. Pei, H. Geng, Y. Huang and T. Zhang, *J. Catal.*, 2016, **333**, 227–237.
- 23 R. Zhang, B. Wang, H. Liu and L. Ling, *J. Phys. Chem. C*, 2011, **115**, 19811–19818.
- 24 J. Lee, D. C. Sorescu and X. Y. Deng, *J. Am. Chem. Soc.*, 2011, **133**, 10066–10069.
- 25 L. Liu, C. Zhao and Y. J. Li, *J. Phys. Chem. C*, 2012, **116**, 7904–7912.
- 26 J. Z. Y. Tan, Y. Fernández, D. Liu, M. Maroto-Valer, J. Bian and X. Zhang, *Chem. Phys. Lett.*, 2012, **531**, 149–154.
- 27 J. C. Matsubu, S. Zhang, L. DeRita, N. S. Marinkovic, J. G. Chen, G. W. Graham, X. Pan and P. Christopher, *Nat. Chem.*, 2017, **9**, 120–127.
- 28 T. Huizinga, H. F. J. van 't Blik, J. C. Vis and R. Prins, *Surf. Sci.*, 1983, **135**, 580–596.
- 29 Z. Xu, J. Yu and M. Jaroniec, *Appl. Catal., B*, 2015, **163**, 306–312.
- 30 T. Yang, Y. Huo, Y. Liu, Z. Rui and H. Ji, *Appl. Catal., B*, 2017, **200**, 543–551.
- 31 X. Zou, Z. Rui, S. Song and H. Ji, *J. Catal.*, 2016, **338**, 192–201.
- 32 J. Graciani, K. Mudiyansele, F. Xu, A. E. Baber, J. Evans, S. D. Senanayake, D. J. Stacchiola, P. Liu, J. Hrbek, J. Fernandez Sanz and J. A. Rodriguez, *Science*, 2014, **345**, 546–550.
- 33 X. Wang, Y. Hong, H. Shi and J. Szanyi, *J. Catal.*, 2016, **343**, 185–195.
- 34 X. Wang, H. Shi and J. Szanyi, *Nat. Commun.*, 2017, **8**, 513.
- 35 D. Heyl, U. Rodemerck and U. Bentrup, *ACS Catal.*, 2016, **6**, 6275–6284.
- 36 P. S. Eckle, H.-G. Anfang and R. J. Behm, *J. Phys. Chem. C*, 2011, **115**, 1361–1367.
- 37 R. Zhang, G. Wang, B. Wang and L. Ling, *J. Phys. Chem. C*, 2014, **118**, 5243–5254.
- 38 Y. H. Zhao, K. Sun, X. Ma, J. Liu, D. Sun, H. Y. Su and W. X. Li, *Angew. Chem., Int. Ed. Engl.*, 2011, **50**, 5335–5338.
- 39 G. Prieto, P. Concepción, A. Martínez and E. Mendoza, *J. Catal.*, 2011, **280**, 274–488.
- 40 J. Wang, G. Li, Z. Li, C. Tang, Z. Feng, H. An, H. Liu, T. Liu and C. Li, *Sci. Adv.*, 2017, **3**, e1701290.
- 41 I. A. Fisher and A. T. Bell, *J. Catal.*, 1997, **172**, 222–237.
- 42 A. Goguet, F. C. Meunier, D. Tibiletti, J. P. Breen and R. Burch, *J. Phys. Chem. B*, 2004, **108**, 20240–20246.
- 43 M. A. Natal-Santiago and J. A. Dumesic, *J. Catal.*, 1998, **175**, 252–268.
- 44 Y. Dai, S. Liu and N. Zheng, *J. Am. Chem. Soc.*, 2014, **136**, 5583–5586.
- 45 Q. Sun, B. Aguila, G. Verma, X. Liu, Z. Dai, F. Deng, X. Meng, F.-S. Xiao and S. Ma, *Chem*, 2016, **1**, 628–639.
- 46 F. Liu, W. Kong, C. Qi, L. Zhu and F.-S. Xiao, *ACS Catal.*, 2012, **2**, 565–572.
- 47 J.-D. Lin, Q.-Y. Bi, L. Tao, T. Jiang, Y.-M. Liu, H.-Y. He, Y. Cao and Y.-D. Wang, *ACS Catal.*, 2017, **7**, 1720–1727.
- 48 G. Huang, Q. Yang, Q. Xu, S. Yu and H. Jiang, *Angew. Chem., Int. Ed.*, 2016, **55**, 7379–7383.
- 49 T. Yang, Y. Huo, Y. Liu, Z. Rui and H. Ji, *Appl. Catal., B*, 2017, **200**, 543–551.
- 50 Y. H. Peng, L. B. Wang, Q. Q. Luo, Y. Cao, Y. Z. Dai, Z. L. Li, H. L. Li, X. S. Zheng, W. S. Yan, J. L. Yang and J. Zeng, *Chem*, 2018, **4**, 613–625.
- 51 Q. Huang and L. Gao, *Chem. Lett.*, 2003, **32**, 638–639.
- 52 Q. Zhang and L. Gao, *Langmuir*, 2003, **19**, 967–971.

